Title

Geometric validation of self-gating k-space-sorted 4D-MRI vs 4D-CT using a respiratory motion phantom

Permalink

https://escholarship.org/uc/item/2m2471jt

Journal

Medical Physics, 42(10)

ISSN

0094-2405

Authors

Yue, Yong
Fan, Zhaoyang
Yang, Wensha
et al.

Publication Date

2015-09-15

DOI

10.1118/1.4929552

Peer reviewed

Geometric validation of self-gating *k*-space-sorted 4D-MRI vs 4D-CT using a respiratory motion phantom

Yong Yue[a)]
Department of Radiation Oncology, Cedars-Sinai Medical Center, Los Angeles, California 90048

Zhaoyang Fan
Department of Biomedical Sciences, Biomedical Imaging Research Institute, Cedars-Sinai Medical Center, Los Angeles, California 90048

Wensha Yang
Department of Radiation Oncology, Cedars-Sinai Medical Center, Los Angeles, California 90048

Jianing Pang
Department of Biomedical Sciences, Biomedical Imaging Research Institute, Cedars-Sinai Medical Center, Los Angeles, California 90048

Zixin Deng
Department of Biomedical Sciences, Biomedical Imaging Research Institute, Cedars-Sinai Medical Center, Los Angeles, California 90048 and Department of Bioengineering, University of California, Los Angeles, California 90095

Elizabeth McKenzie, Richard Tuli, and Robert Wallace
Department of Radiation Oncology, Cedars-Sinai Medical Center, Los Angeles, California 90048

Debiao Li
Department of Biomedical Sciences, Biomedical Imaging Research Institute, Cedars-Sinai Medical Center, Los Angeles, California 90048 and Department of Bioengineering, University of California, Los Angeles, California 90095

Benedick Fraass
Department of Radiation Oncology, Cedars-Sinai Medical Center, Los Angeles, California 90048

Purpose: MRI is increasingly being used for radiotherapy planning, simulation, and in-treatment-room motion monitoring. To provide more detailed temporal and spatial MR data for these tasks, we have recently developed a novel self-gated (SG) MRI technique with advantage of *k*-space phase sorting, high isotropic spatial resolution, and high temporal resolution. The current work describes the validation of this 4D-MRI technique using a MRI- and CT-compatible respiratory motion phantom and comparison to 4D-CT.

Methods: The 4D-MRI sequence is based on a spoiled gradient echo-based 3D projection reconstruction sequence with self-gating for 4D-MRI at 3 T. Respiratory phase is resolved by using SG *k*-space lines as the motion surrogate. 4D-MRI images are reconstructed into ten temporal bins with spatial resolution $1.56 \times 1.56 \times 1.56$ mm^3. A MRI-CT compatible phantom was designed to validate the performance of the 4D-MRI sequence and 4D-CT imaging. A spherical target (diameter 23 mm, volume 6.37 ml) filled with high-concentration gadolinium (Gd) gel is embedded into a plastic box ($35 \times 40 \times 63$ mm^3) and stabilized with low-concentration Gd gel. The phantom, driven by an air pump, is able to produce human-type breathing patterns between 4 and 30 respiratory cycles/min. 4D-CT of the phantom has been acquired in cine mode, and reconstructed into ten phases with slice thickness 1.25 mm. The 4D images sets were imported into a treatment planning software for target contouring. The geometrical accuracy of the 4D MRI and CT images has been quantified using target volume, flattening, and eccentricity. The target motion was measured by tracking the centroids of the spheres in each individual phase. Motion ground-truth was obtained from input signals and real-time video recordings.

Results: The dynamic phantom has been operated in four respiratory rate (RR) settings, 6, 10, 15, and 20/min, and was scanned with 4D-MRI and 4D-CT. 4D-CT images have target-stretching, partial-missing, and other motion artifacts in various phases, whereas the 4D-MRI images are visually free of those artifacts. Volume percentage difference for the 6.37 ml target ranged from $5.3\% \pm 4.3\%$ to $10.3\% \pm 5.9\%$ for 4D-CT, and 1.47 ± 0.52 to 2.12 ± 1.60 for 4D-MRI. With an increase of respiratory rate, the target volumetric and geometric deviations increase for 4D-CT images while remaining stable for the 4D-MRI images. Target motion amplitude errors at different RRs were measured with a range of 0.66–1.25 mm for 4D-CT and 0.2–0.42 mm for 4D-MRI. The results of Mann–Whitney tests

indicated that 4D-MRI significantly outperforms 4D-CT in phase-based target volumetric ($p = 0.027$) and geometric ($p < 0.001$) measures. Both modalities achieve equivalent accuracy in measuring motion amplitude ($p = 0.828$).

Conclusions: The *k*-space self-gated 4D-MRI technique provides a robust method for accurately imaging phase-based target motion and geometry. Compared to 4D-CT, the current 4D-MRI technique demonstrates superior spatiotemporal resolution, and robust resistance to motion artifacts caused by fast target motion and irregular breathing patterns. The technique can be used extensively in abdominal targeting, motion gating, and toward implementing MRI-based adaptive radiotherapy. © 2015 American Association of Physicists in Medicine. [http://dx.doi.org/10.1118/1.4929552]

Key words: 4D-MRI, 4D-CT, tumor motion, respiratory gating, motion phantom

1. INTRODUCTION

Four-dimensional (4D) computed tomography (CT) is currently a standard in radiotherapy planning to assess respiratory motion and determine treatment margins for target tumors.[1–3] An internal target volume (ITV), derived from the union volumes of all breathing phases or a maximum intensity projection, is typically used to derive the planning target volume (PTV) for the majority of treatment planning and delivery techniques in which motion is an issue. Use of an ITV generally provides an adequate margin on the target, however, it may also lead to increased potential toxicity to surrounding healthy tissue.

Phase-resolved target definition and motion management are highly desired in clinical practice.[4,5] However, implementation of phase-resolved imaging has several technical difficulties due to the limitations of current acquisition hardware and respiratory phase reconstruction software, especially for reconstruction based on retrospective sorting of sequential axial acquisitions of 3D-CTs using an external respiratory surrogate.[6] This imaging process is prone to manifest motion artifacts caused by irregular breathing patterns, and low spatiotemporal resolution. It has been reported that 90% of scans have at least one artifact in a retrospective study on 50 patients with lung and abdominal tumors.[7]

Recent developments in 4D-MRI techniques provide alternative solution(s) to the motion assessment problems in radiotherapy. Various early efforts have been made toward developing real-time 3D volumetric acquisition,[8–12] however, the trade-off between spatial and temporal resolution has limited its application in tumor targeting and motion assessment. An alternative strategy has been recently proposed which will improve the frame rate and in-plane spatial resolution based on respective sorting of 2D multislice acquisitions.[13–17] However, the slice resolution must remain relatively low (i.e., 3–10 mm) in order to maintain satisfactory 2D slice profile and signal or to reduce the total scan time. More importantly, the image reconstruction, similar to 4D-CT, still relies on sorting of postreconstructed slice images, so it is vulnerable to irregular breathing and anisotropic spatial resolution, and may suffer target stretching and partial missing artifacts.[18,19] Therefore, currently available 4D techniques have limited ability to provide an optimal solution for phase-resolved target imaging in radiotherapy.

We have recently reported a novel 4D MRI method based on self-gating motion surrogate and retrospective *k*-space sorting.[20–22] The 4D acquisition is completed in a fixed scan time and provides both high spatial and high temporal resolution. This approach resolves the respiratory phase sorting and reconstruction all in *k*-space. One of the important advantages of the technique is that the phase sorting is self-gated without prescan selection or in-scan external respiratory surrogate acquisition. This technique allows the removal of motion outliers and artifacts without interrupting the acquisition.[22] Another major advantage of the technique is that it provides isotropic high spatial resolution, which enables accurate evaluation of phase-based target definition and motion measurement.

The goal of the current study is to conduct a geometric validation of the 4D MRI technique using a MRI/CT compatible respiratory motion phantom, and to compare the 4D MRI technique to 4D CT using the motion phantom. Clinical imaging results and a description of the imaging sequence development have been reported in Ref. 22, and a manuscript describing clinical evaluation of the sequence for radiotherapy use in pancreatic cancer is in preparation.

2. METHODS

2.A. 4D-MRI acquisition

The 4D-MRI sequence is based on spoiled gradient echo-based 3D projection reconstruction (PR) sequence with self-gating (SG) at 3 T.[22,23] Figure 1 illustrates the flowchart of 4D image acquisition. Radial projections in *k*-space are continuously collected in a 2D golden means ordering[24] that allows for flexible retrospective data sorting. The respiration-induced shift of the imaging target is recorded by a group of two superior-inferior (SI) *k*-space projections (i.e., SG lines), which are inserted every 15 radial projections (i.e., imaging lines). The temporal interval between two SG lines is approximately 98 ms [Fig. 1(a)]. A total of 86 160 radial projections and 5744 SG lines are obtained in 8 min in the scans used in the current study. The 8 min acquisition time was determined to provide an adequate number of *k*-space projections based on our earlier work in human abdominal imaging studies.[22]

Respiratory phase is resolved by extracting the respiratory signal from SG lines. The Fourier transform of a SG line represents a 1D projection of the entire imaging volume. The respiratory motion signal was extracted by applying principal component analysis (PCA) to the projection profile time series
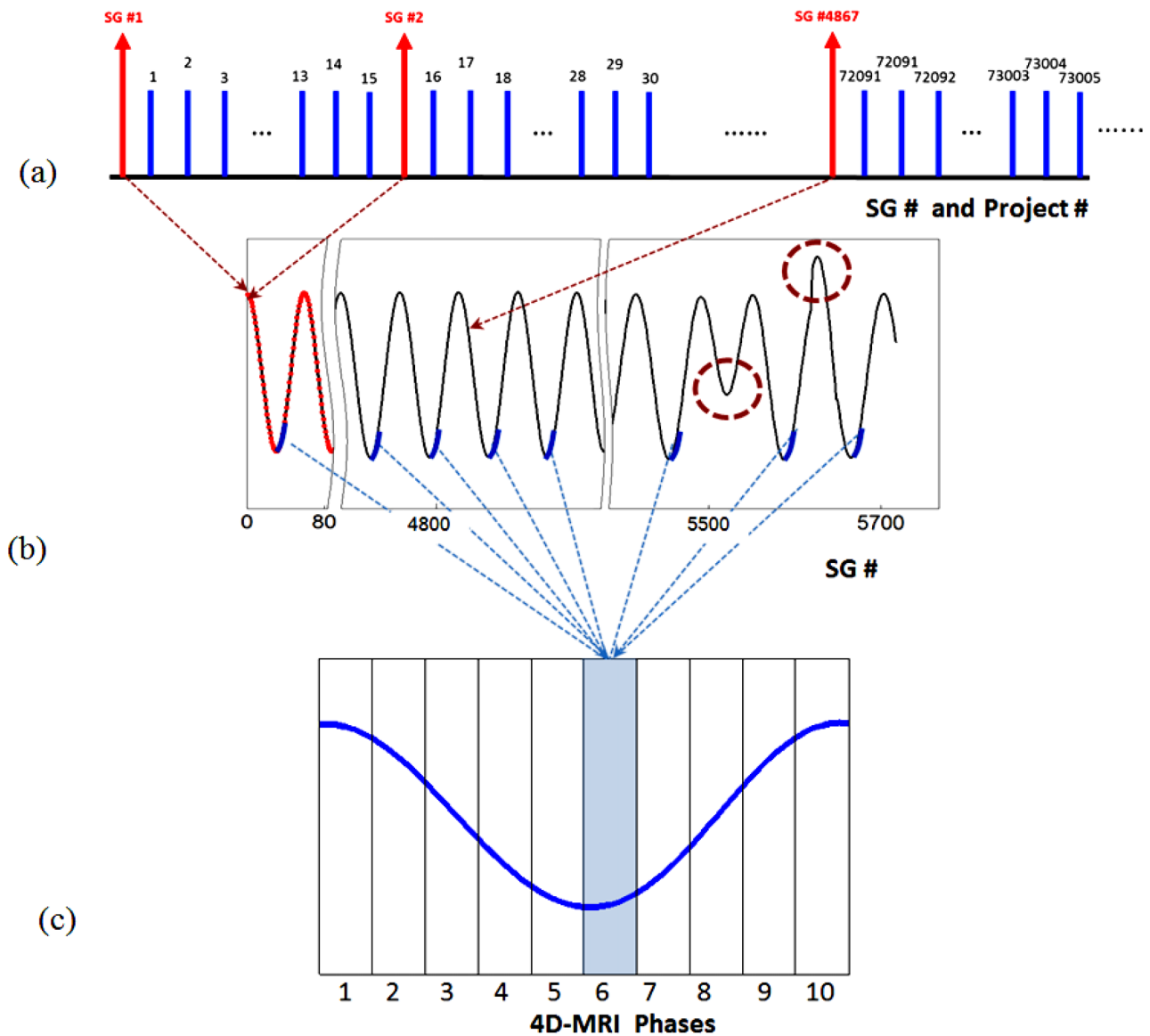
Fig. 1. The flow chart for 4D-MRI acquisition and phase sorting of reconstruction. (a) Image sequence with *k*-space segments, consisting of SG and 15 radial projection lines, giving a temporal interval of ~98 ms between each SG line. A total of 86 160 projections were collected with 5744 SG lines after an approximately 8 min scan. (b) The SI respiratory curve is extracted by the PCA-based method. As shown in the left side curve, each point (in solid dot) represents a SG line (indicated by arrows). Many SG lines contribute one cycle of the respiratory curve. The resultant curve represents the respiratory motion through the entire imaging acquisition. (c) The respiratory cycle is divided into ten phases. The projections with the same phase number (shown in solid segments) are assigned to a resolved phase in 4D (shown in shade). Furthermore, motion artifact removal is built in to the reconstruction. Any abnormal segments [shown in circled segments in (b)] will be excluded from reconstruction.

from all channels.[23,25] As shown in Fig. 1(b), the respiratory motion of the target is plotted as the relative SI displacement derived from SG lines. On this curve, the respiratory cycles are identified by the time period of two neighbor expiratory peaks. Motion is sampled by SG every 98 ms (i.e., $17 \times$ TR, due to the acquisition of 15 imaging lines and two SG lines), which is much shorter than the typical respiratory cycle lengths (>4 s, typically).

To sort the phase data, respiratory cycles are temporally evenly divided into 10 bins. The *k*-space data with the same phase number for all respiratory cycles are assigned to a final nominal phase bin. As shown in Fig. 1(c), the phase information of each bin (e.g., bin-6) is contributed by that same bin (e.g., all bin-6s) for all validated cycles [Fig. 1(b)]. To suppress

motion artifacts, segments with the abnormal time period or inconsistent positions (≥mean± two standard deviations) are considered to be outliers [e.g., dashed-circles in Fig. 1(c)], and are excluded from phase binning. After sorting *k*-space data, the image of each individual phase is reconstructed using a self-calibrating sensitivity encoding (SENSE) reconstruction method,[23] which uses the receiver coil sensitivity information to suppress aliasing artifacts. No other correction, such as bias field, was used in the 4D reconstruction.

In the phantom experiments, the cubic imaging volume of 4D-MRI was centered on the moving phantom with the following imaging parameters: FOV ($300 \times 300 \times 300$ mm^3), spatial resolution ($1.56 \times 1.56 \times 1.56$ mm^3), flip angle (10°), TR/TE = 5.8/2.6 ms, readout bandwidth = 399 Hz/pixel, nonselective

water excitation RF pulse. The reconstructed 4D-MRI image set consists of ten temporal phases.

2.B. MRI-CT respiratory motion phantom

A MRI-CT compatible phantom was designed to validate the performance of the 4D MRI sequence and 4D CT imaging. A spherical target (diameter 23 mm, volume 6.37 ml) filled with high-concentration gadolinium (Gd) gel was embedded into a plastic box ($35 \times 40 \times 63$ mm^3) and stabilized with low-concentration Gd gel [Fig. 2(e)]. The plastic box was further stabilized with plastic supports and sealed into a water container. The phantom was designed to have similar contrast between target and background for both MRI and CT imaging.

The phantom can produce superior-inferior motion driven by an air pump which is placed outside the MRI room. Human respiratory motion was mimicked using the controller module of the dynamic breathing phantom (RSD TM), which has the capability to produce various human respiratory rates (2–20 s/cycle) and breathing depths (3–30 mm). The RSD controller model is able to provide two respiratory signals (Fig. 2): pressured air generated by the air pump and mechanical motion generated by the linear actuator. The former is used to drive the phantom in the SI direction during both CT and MRI scans, and the latter output is used to drive the motion surrogate in the anterior–posterior (AP) direction for 4D-CT scans. In our experiments, the motion system simulated the human breathing patterns using diaphragm motion (target) and chest wall motion (RPM box). To achieve this, the external surrogate (RPM box) was driven by the same respiratory rate and amplitude of target input signal but with 90° phase shift, as shown Fig. 2. Before experiments, the system was calibrated to synchronize the two motions and this synchronization was further verified with video recordings. Therefore, motion artifacts due to uncoordinated external surrogate motion were eliminated.

The respiratory rates and depth were calibrated by tuning the controller parameter and adjusting input and output air volume. The calibrated curve as a function of respiratory rate and depth is shown Fig. 3. As a result, the phantom is able to produce human-type breathing patterns between 4 and 30 respiratory cycles/min. In addition, the RR is inversely proportion to breathing depth: it can produce a fast respiration rate with shallow breathing depth (e.g., 30/min, 2 mm), and a slow respiration rate with deep breathing (e.g., 6/min, 20 mm). Four respiratory rate settings, 6, 10, 15, and 20/min, were selected to be used in MRI and CT acquisitions with their corresponding respiratory cycle times and depths of 10 s/20 mm, 6 s/15 mm, 4 s/10 mm, and 3 s/7 mm. During scans, the ground truth for the motion was obtained from input signals and validated by real-time video recordings.
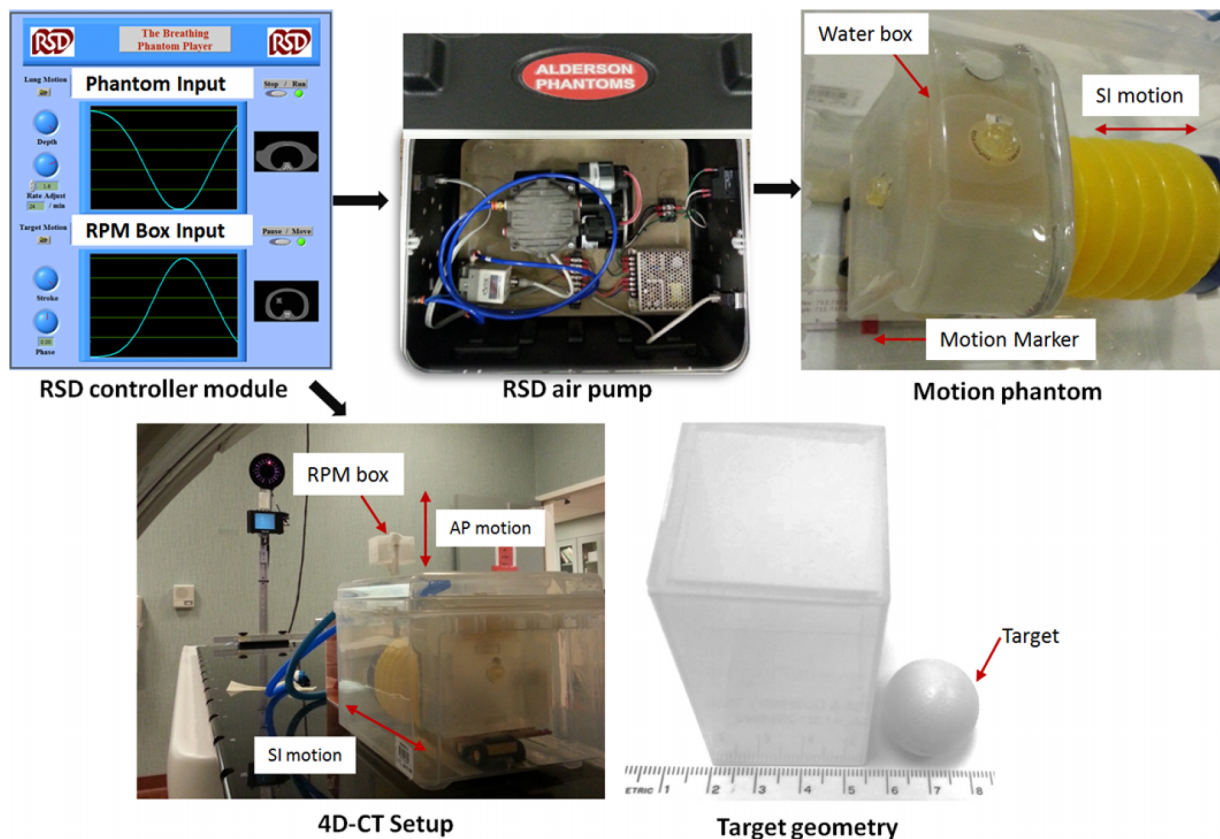

FIG. 2. Dynamic MRI phantom and experiment setup. The phantom is driven by a commercial RSD controller module with two motion outputs: the modulated pressure air generated by air pump, and mechanical motion generated by a linear actuator. The former is used to drive the target, and the latter is used to drive an external surrogate (RPM box) during 4D-CT acquisition. The target is filled with high-concentration Gd-gel, and is stabilized in a plastic box. The plastic box is filled with low-concentration Gd-gel, and further is embedded in a water box.
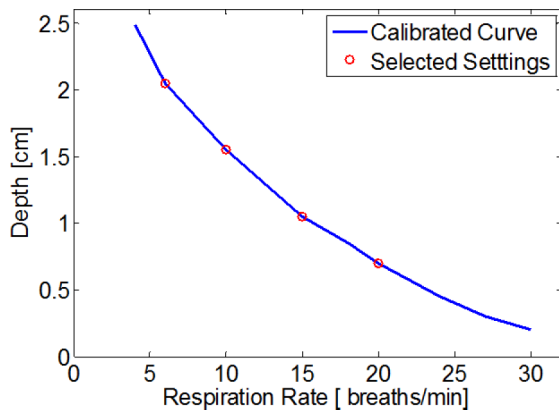
Fig. 3. Motion calibration curve of the dynamic phantom as a function of RR. The red circles indicate that four RR settings (6, 10, 15, and 20) are used in this study.

2.C. 4D CT acquisition

4D CT images were acquired using a GE CT590 CT scanner with cine mode. Before each 4D-CT, the phantom was scanned in helical mode to acquire a static 3D image. During the 4D-CT scans, a linear actuator operated by the RSD motion controller was used to produce external respiratory AP motion. As shown in Fig 2(d), a RPM plastic box labeled with infrared markers was placed on the tip of the line actuator, where it can be tracked by the Varian RPM system during 4D-CT scans. The AP motion of the linear actuator was set to be 90° (orthogonal) to the SI motion of output of air pump.

Images were acquired for a cine duration that was set to 1.5 s longer than the estimated respiratory period from the RPM system. Scan parameters were set as follows: 1 s gantry rotation, 0.2 s cine interval. The slice thickness was set to 2.5 mm for motion ranges larger than 2.0 cm, and 1.25 mm for those 2.0 cm or less. The 4D-CT images were reconstructed by GE Advantage 4D software. Specifically, raw 4D-CT cine images were sorted retrospectively into respiratory phase-based bins. Each CT slice in the raw cine images was assigned a phase number according to the temporal correlation between the RPM trace and CT data acquisition. Then, the images with the same phase were used to construct 3D-CT data sets, and sorted retrospectively into ten respiratory phases (i.e., from 0% to 90% phase at 10% intervals).

2.D. Motion and geometric qualification

The 4D-CT and MRI images were imported into a treatment planning system (Varian Eclipse v11.0) and an image segmentation software [ITK-SNAP (Ref. 26)] for geometric qualification. Four dimensional structure sets were created for the 4D-CT and 4D-MRI scan sets using the 4D-CT module in ECLIPSE. The target motion visualized with the CT and MRI 4D image sets was tracked through the positions of centroids of spheres in each individual phase in each dataset. Meanwhile, the ground truth positions of the sphere were measured in the recorded video and real-time 2D MRI sequence images.

Contours of the sphere targets were manually drawn for all the phase-resolved images by two users. Based on the drawn contours, the volumes were measured using the software. The ground truth volume of the sphere (V_{GT}) was calculated from the physical parameters (diameter 2.3 cm, volume 6.37 ml), and validated by the static helical 3D-CT image. For the 4D images, the volume deviations were calculated by comparing the volume difference between measurements and the ground
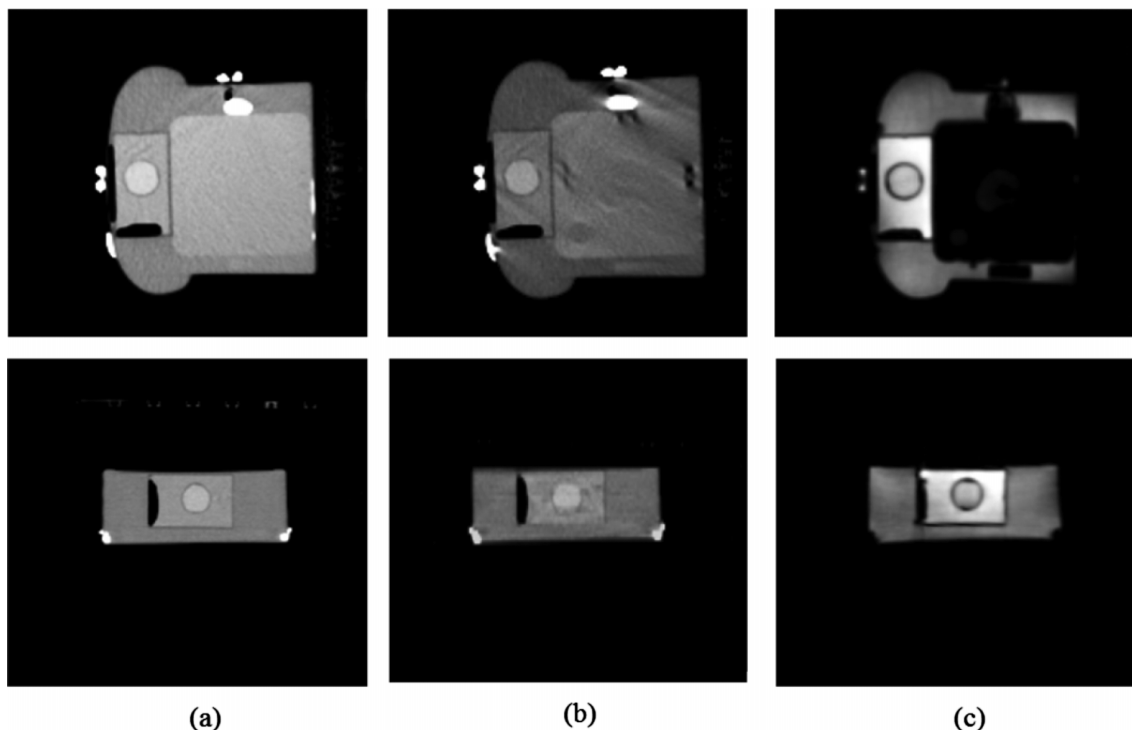

Fig. 4. Phantom images in axial (top) and coronal (bottom) views. (a) Static 3D-CT image, compared with phase resolved (b) 4D-CT image, and (c) 4D-MRI image.

truth volume, $dV = V_{\text{Measured}} - V_{\text{GT}}$, and the percentage of difference $dV\% = (V_{\text{Measured}} - V_{\text{GT}})/V_{\text{GT}}$, as well as its absolute percentage difference $|dV\%|$. Here, we assumed that volume deviation represents motion-introduced errors in the gross tumor volume (GTV) on actual patient 4D CT or MRI scans.

To examine the geometrical accuracy of the target representation, the imaged targets were further characterized as a spheroid with semimajor axis length, a, and semiminor axis length, b. To obtain the axis lengths, the DICOM structure sets containing the contours of each individual phase were exported and postprocessed in MATLAB (TM, v8.1). Two geometric parameters of the spherical targets, flattening and eccentricity, were calculated. The flattening (F) measures the ratio of the difference of the two axis lengths to the semimajor axis length $F = (a - b)/a$, and eccentricity (E) describes the deviation from being circular, $E = \sqrt{a^2 - b^2}/a$. Finally, the
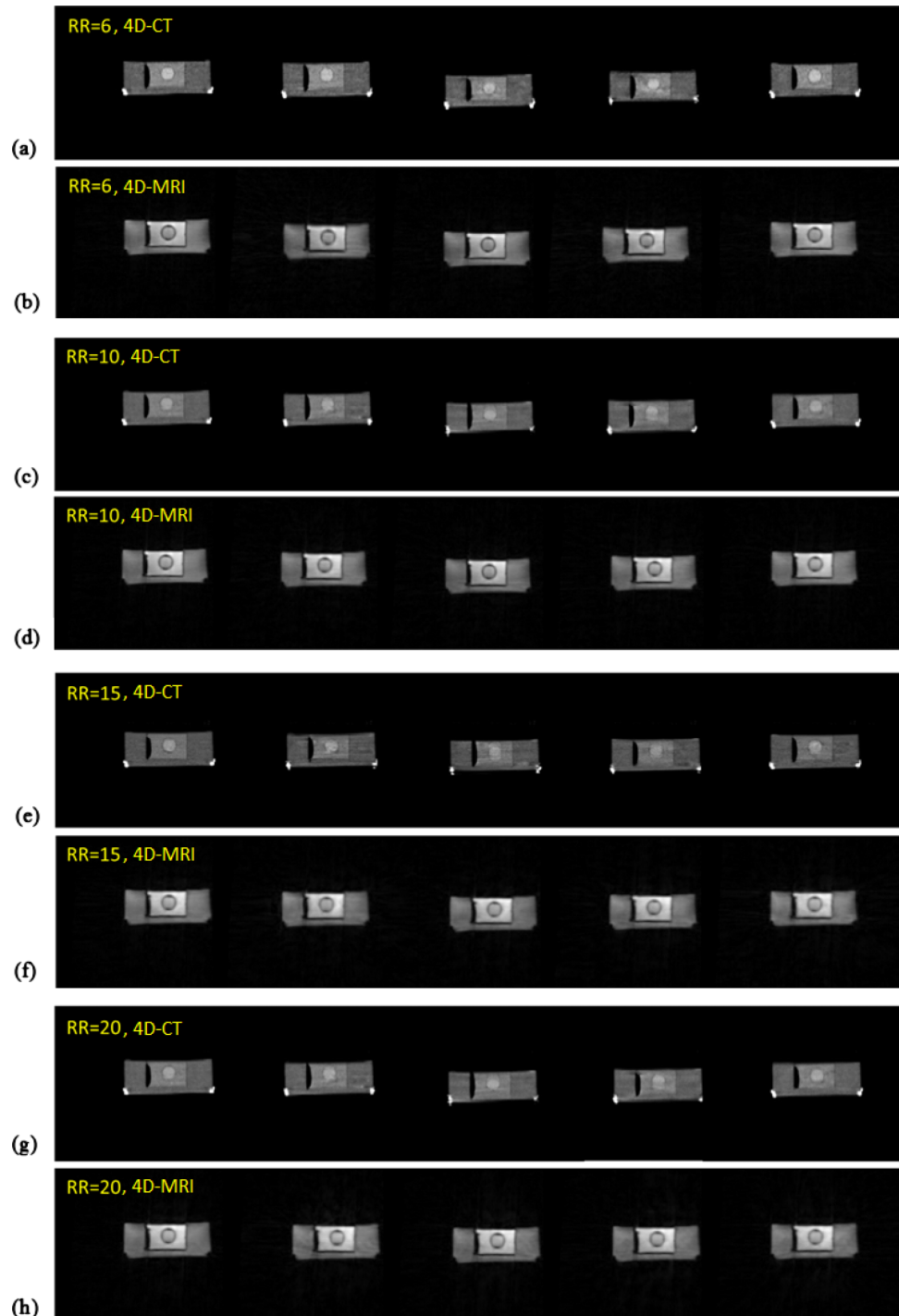

FIG. 5. Phase-resolved 4D phantom images are demonstrated by phase 1, 3, 5, 7, and 9. The 4D-CT images [(a), (c), (e), and (g)] are compared with 4D-MRI images [(b), (d), (f), and (h)] at four different respiratory rates (RR = 6, 10, 15, and 20).

Mann–Whitney test (*U*-test) was used to compare the performance of 4D MRI and CT in both motion tracking and phase-based target definition.

3. RESULTS

3.A. Results of phase-resolved reconstruction

4D MRI and 4D CT scans were acquired for the dynamic phantom operated with four RRs: 6, 10, 15, and 20/min. Each 4D scan was reconstructed into ten phases. Figure 4 illustrates phase-resolved images from the 4D-CT and 4D-MRI datasets of the phantom, compared with its static 3D-CT image. As shown in the figure, the sphere targets in the CT images have similar gray level and contrast as the ones in the MRI images.

Figure 5 visually demonstrates the differences between the 4D-CT and MRI images, using images from individual phases 1, 3, 5, 7, and 9 and acquired at different respiratory rates. As shown, 4D-CT images in Figs. 5(a) and 5(c), 5(e), and 5(g), the images of phase 1 are visually similar to the static

image, whereas other phase images appear to have more or less motion artifact, e.g., target stretching (phase 5, RR = 15), and squeezing or partially missing information (phase 3, RR = 15). It is also apparent that images acquired during slow motion mode (RR = 6) appear to have fewer artifacts.

In contrast to the 4D-CT, the phase-resolved 4D-MRI images do not have similar motion artifacts to those seen in the 4D-CT images. As shown in 4D-MRI, in Figs. 5(b) and 5(d), 5(f) and 5(h), all images at different phases and different respiratory rates have nearly equivalent image quality (e.g., compare the phase 3 at RR = 20 4D-MRI vs the phase 3 4D-MR image at RR = 6). The results indicate that 4D-MRI has robust spatial–temporal resolution at various respiratory rates.

3.B. Results of phase-resolved geometry measures

The target volumes were contoured and measured in both planning and segmentation software by two users. The results of Wilcoxon tests indicated that there was no significant
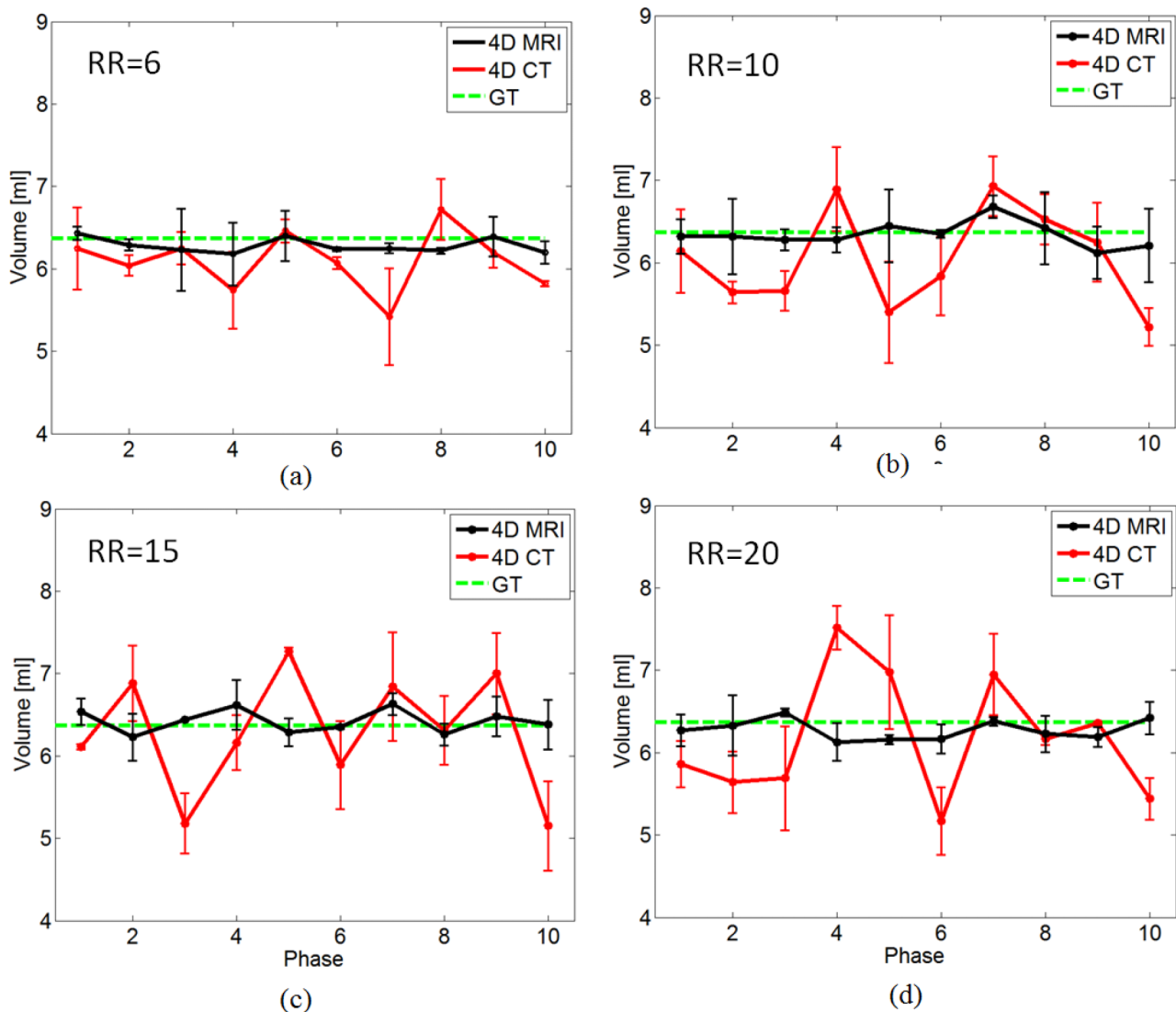

FIG. 6. Phase-resolved target volume is compared between 4D-MRI and 4D-CT at different RRs. (a) RR = 6, (b) RR = 10, (c) RR = 15, and (d) RR = 20. The ground truth (green dashed line) is 6.37 ml.

difference between contours drawn by different operators (p = 0.0003 for CT images, $p << 0.0001$ for MRI images). Figure 6 shows the measured volumes plotted as a function of phase. For the same RR setting, target volumes in 4D-MRI are very close to the ground-truth volume, whereas some phases of 4D-CT demonstrate a large volume measurement error. As shown in CT images of Fig. 5(f) for RR = 15, the target sphere is truncated at phase 3 (5.18 ml), whereas it is stretched at phase 5 (7.27 ml). This is due to motion artifact and phase-sorting error in the 4D-CT reconstruction. Given the ground-truth volume (6.37 ml), the percentage deviations of volume ($dV\%$) for four settings were calculated, shown in Fig. 7.

Table I summarizes the performance of the 4D-CT and 4D-MRI in phase-resolved volume measurement. For 4D-CT, the absolute volume error increases with increasing respiratory rate, from 5.3% ± 4.3% (RR = 6) to 10.3% ± 5.9% (RR = 20). The minimum and maximum phase-resolved volumes also show the same trend. For 4D-MRI, volumetric errors at different RRs are all smaller than 3%, and are independent of the respiratory rates. Combining all RR settings, the overall volumetric errors are 8.4% ± 5.6% for 4D-CT and 1.8% ± 1.3% for 4D-MRI. The Mann-Whitney test was used to examine the statistical difference of the 4D-CT and 4D-MRI in terms of volume measurement, with a result of $p = 0.027$.

The results of the flattening and eccentricity metrics in 4D-CT and 4D-MRI are compared in Table II. Similar to the trend of the volume measurements, the mean values of flattening and eccentricity for 4D-CT also increase with increasing respiratory rate. The results indicate that fast target speed introduces more motion artifacts, causing large deviation from the original sphere shape. For 4D-MRI, however, the geometric deviations are both much smaller than the results from 4D-CT, and remain stable when the respiratory rate increases. The results of Mann–Whitney tests on the two parameters, $p = 0.001$ for flattening, and $p = 0.0005$ for eccentricity, suggest that the performance of 4D-CT and 4D-MRI is significantly different. Together with the volume measurements, the overall results suggest the proposed 4D MRI is significantly superior

to CT in term of phase-based target definition and geometric measures.

3.C. Results of phase-resolved motion detection

The target motion was measured by tracking the centroid of sphere of each individual phase. The ground truth for the motion was obtained from input signal and video recording. To evaluate the comparison of the methods, motion phase and amplitude of targets were measured. Figure 8 shows the phase-resolved target positions measured by 4D-CT and 4D-MRI versus the ground truth. With increase of RRs, the inhale phase (the valley on the curve) shifts to the center (from phase 6 to phase 5) of the curve. Overall, motion phase detected by each of the two modalities matches the ground truth well.

Motion amplitudes at different respiratory rates have been calculated, and are listed in Table III. The motion amplitude decreases with increase of respiratory rate, ranging from 7.7 to 20.1 mm. The results suggest that the two modalities achieve similar accuracy in terms of detection of motion amplitudes, although the values from the 4D-MRI are numerically better. Note that the spatial resolution of the 4D-CT [$1.27 \times 1.27 \times 1.25$ mm] at RR = 10, 15, and 20 is comparable to the resolution of the 4D-MRI [$1.56 \times 1.56 \times 1.56$ mm], except the slice thickness for the RR = 6 4D-CT scans has to be increased to 2.5 mm due to the scan coverage requirements.

The Mann-Whitney test shows that the motion detection using the 4D MRI was statistically equivalent to that with 4D CT ($p = 0.828$). In summary, the results indicate 4D MRI can be used to accurately define target geometry and volume in each phase, and equivalent (or better) performance with 4D CT for measuring target motion range.

4. DISCUSSION

MR imaging has been used extensively for treatment planning of radiation therapy due to its advantage of improved soft-tissue contrast. Since no ionization is involved, MRI can provide a comprehensive therapy imaging solution for diag-
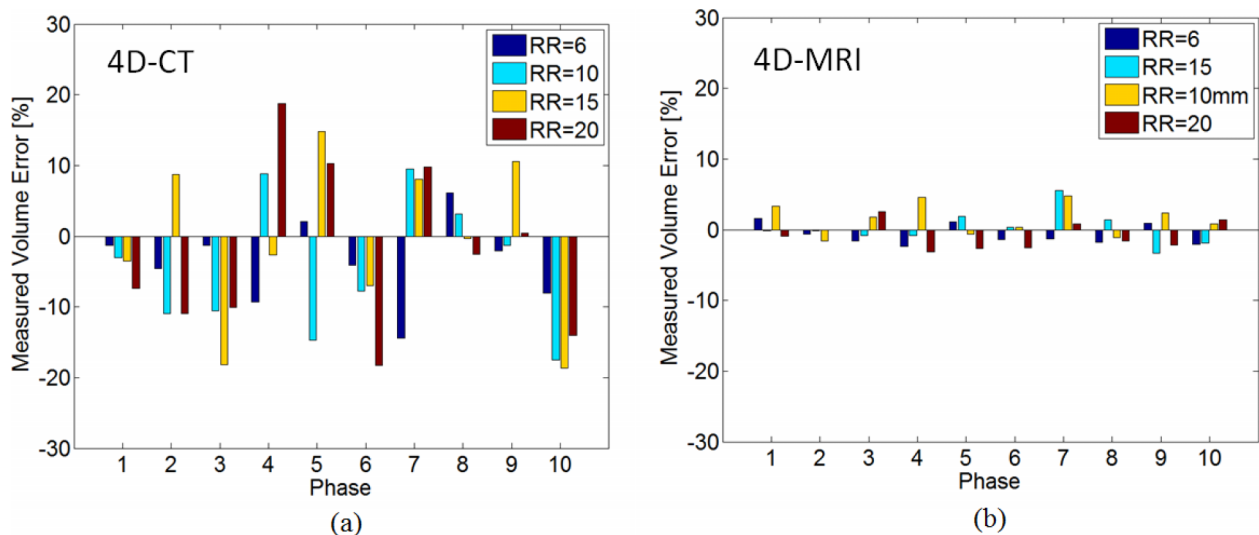

Fig. 7. Phase-resolved target volume measurement errors dV at different respiratory rates (RR = 6, 10, 15, and 20). (a) 4D-CT and (b) 4D-MRI.

TABLE I. Target volumes measured by phase-resolved 4D-MRI and 4D-CT images. The accuracy is evaluated by the percentage deviation to the ground truth (6.37 ml), and is illustrated by minimum and maximum volumes.

Phantom respiratory rate per min	Ground truth volume (ml)	4D-CT target volume (ml)		4D-CT volume error $|dV|$ (%)	4D-MRI target volume (ml)		4D-MRI volume error $|dV|$ (%)
		Min	Max		Min	Max	
6	6.37	5.42	6.72	5.3 ± 4.3	6.18	6.43	1.5 ± 0.5
10	6.37	5.22	6.93	8.7 ± 5.2	6.12	6.68	1.6 ± 1.7
15	6.37	5.15	7.27	9.2 ± 6.4	6.23	6.63	2.1 ± 1.6
20	6.37	5.17	7.52	10.3 ± 5.9	6.13	6.49	1.8 ± 1.0

nosis, planning, in-treatment-room monitoring, and therapy response evaluation without radiation dose to the patient. With the recent development of MRI-Linacs and other MRI-based therapy systems,[27–30] MRI-based methods for in-treatment-room monitoring are going to be very important for these systems. Concurrently, intensive efforts are also being devoted to using MRI as the primary simulation and planning imaging modality for radiotherapy in a number of clinical sites.[31–33] In any scenario utilizing MRI for simulation, planning and/or treatment guidance, accurate 4D-MRI would be an essential component of motion management in the clinical use of MRI-guided or monitored radiotherapy.

Several techniques for 4D-MR have recently been proposed.[8–17] However, most of these approaches still rely on either external gated or overhead prescans as the motion surrogate, limiting the spatiotemporal resolution and robustness of these methods to motion artifacts. The self-gating-based *k*-space sorted 4D-MR approach described here fundamentally solves these issues in sequence design and reconstruction algorithm. The method features a simplified scanning procedure, inherent motion artifact resistance, high isotropic spatial resolution, and high temporal resolution. This study shows that the proposed 4D-MR method is superior to 4D-CT in terms of defining the target geometry and volume at each individual phase, and provides accurate measurement on motion phase and amplitude while also achieving a high and isotropic resolution in the imaging data.

To our knowledge, this work is the first comprehensive study on quality assurance of 4D-MRI in terms of phase-resolved target geometry and motion using a phantom mimicking human respiratory motion. An important part of this study was the design of a MRI/CT compatible phantom. The goal of the design was to create a phantom which was equally relevant to either imaging modality. A water-gel mixture was used because it provides a typical background soft-tissue signal for both CT and MR. To produce contrast in the target,

high-concentration Gd was diluted in the target sphere, in order to create better SNR for both CT and MR. The plastic outside of the target also ensured a clearly defined boundary for both CT and MRI. These design decisions were successful at minimizing the image quality differences between the two image modalities.

The 4D-CT results in this study are comparable to the typical 4D-CT phantom studies in the literature. In a cross-institutional study,[19] a commercial Quasar phantom was used in quality assurance of 4D-CT, where two targets with different sizes, 15 mm diameter (1.77 ml) and 30 mm diameter (14.1 ml), were used. Given 1.5 and 2.5 cm motion for RR = 10 and 20, their results showed that the volumetric detection errors in the single phase (mid-ventilation, end-inspiration, and end-expiration) were 13.4%–32.6% for small targets and 2.5%–8.0% for large targets.[19] In the current work, the size of the target is between these two extremes (23 mm diameter, 6.37 ml) and has a mean volumetric error of 5.2%–10.3%. Based on the comparison with 4D-CT, the *k*-space self-gated 4D-MRI reported here (mean volumetric error 1.5%–2.1%) achieves significantly superior performance in defining phase-resolved volumes ($p = 0.027$).

The respiratory rate (an index of target motion velocity) is an import factor for the image quality of 4D images. Our 4D-CT results show that phase-resolved geometric and volumetric deviations increase with an increase of motion velocity. At fast respiratory rates, 4D-CT is more likely to fail to accurately identify the target geometry for each individual phase. This is due to the limitation of the phase-sorting based 4D-CT reconstructions, which rely on the correlation between the external motion surrogate and the real target motion. Compared to 4D-CT, the image quality of 4D-MRI is relatively insensitive of target motion speed. In fact, the fast respiratory rate produces more self-gated signals in a given scanning time (8 min). Therefore, the image quality of 4D-MRI is not affected by motion speed. As shown in Fig. 5, all individual phases in

TABLE II. Geometric parameters measured by phase-resolved 4D-MRI and 4D-CT images.

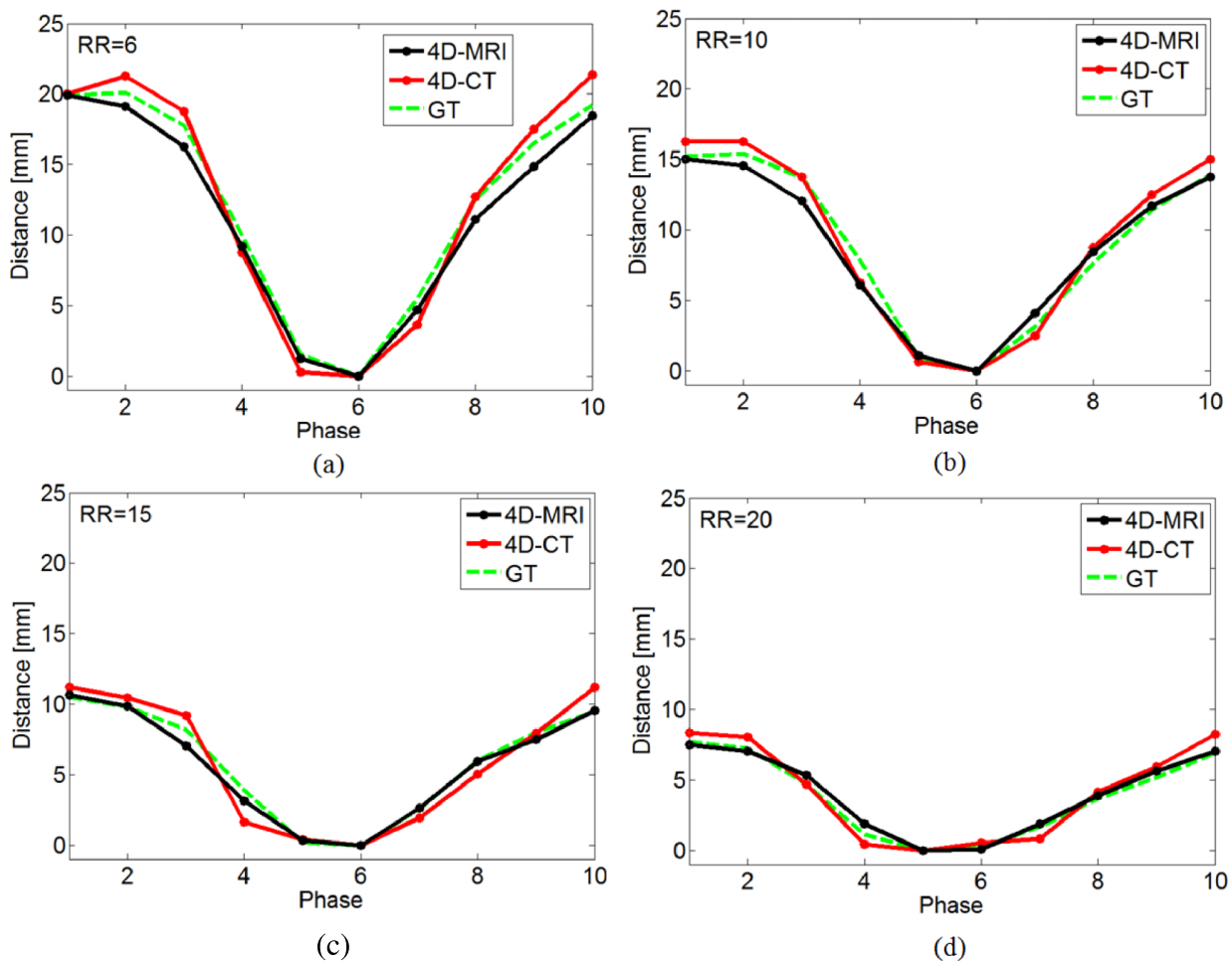| Phantom respiratory rate per min	Flattening (F)				Eccentricity (E)			
	4D-CT		4D-MRI		4D-CT		4D-MRI	
	Max	Mean	Max	Mean	Max	Mean	Max	Mean
6	0.24	0.08 ± 0.06	0.09	0.03 ± 0.04	0.65	0.32 ± 0.22	0.32	0.19 ± 0.15
10	0.25	0.12 ± 0.07	0.10	0.05 ± 0.04	0.66	0.44 ± 0.15	0.33	0.21 ± 0.18
15	0.23	0.13 ± 0.08	0.07	0.05 ± 0.02	0.64	0.46 ± 0.16	0.36	0.25 ± 0.11
20	0.24	0.16 ± 0.07	0.07	0.03 ± 0.02	0.68	0.47 ± 0.13	0.36	0.22 ± 0.12

FIG. 8. Phase-resolved target motion is compared between 4D-MRI and 4D-CT at different RRs. (a) RR = 6, (b) RR = 10, (c) RR = 15, and (d) RR = 20. The ground truth (GT, green dashed line) is measured from video recording.

4D-MRI remain the same quality and nearly free of motion artifacts. Given this merit, target volumes measured at different phase and respiratory rates are all within 5% [Fig. 7(b)]. The image quality for visual comparison also shows that 4D-MRI has excellent artifact-resistance which is phase-independent and motion-independent.

Another factor that may introduce motion artifacts is irregular breathing patterns, which are commonly seen in patients. 4D-CT images are typically reconstructed based on retrospective sorting of sequential axial acquisitions of 3D-CTs using an external respiratory surrogate. Irregular breathing may induce position inconsistency in some slices which are not well correlated to the corrected respiratory phase during retrospective slice sorting. The phase-sorting errors may cause the correct

phase image slice to be replaced by its nearby phase image slices. If the mis-sorting happens at the boundary of a structure (e.g., the target), an extra-boundary slice (target-stretching) or missing-boundary slice (target-squeezing) can be induced into the scanned target.[18,19]

At present, no single 4D-CT scanning system can adequately handle irregular breathing. Several methods have been proposed to reduce this type of motion artifact, for example, audio/video coaching and adapting the scan parameters to the breathing period. Similarly, irregular breathing would potentially pose challenges to retrospective slice sorting-based 4D-MRI techniques. Our 4D-MRI technique is designed to resist the respiratory irregularity.[22] To reduce motion artifacts, the SG-labeled segment signals with abnormal time period or

TABLE III. The motion amplitude measured by 4D-CT and 4D-MRI at different respiratory rates. Here, motion amplitude is the difference between minimum and maximum moving distance, and the ground truth is obtained by measurement of the motion marker in the acquired video.

Phantom respiratory rate per min	Ground-truth motion amplitude (mm)	4D-CT motion amplitude (mm)	4D-CT motion amplitude error (mm)	4D-MRI motion amplitude (mm)	4D-MRI motion amplitude error (mm)
6	20.10	21.35	1.25	19.93	−0.17
10	15.42	16.25	0.83	15.00	−0.42
15	10.50	11.21	0.71	10.62	0.12
20	7.70	8.36	0.66	7.50	0.20

inconsistent position (≥mean ± two standard deviations) are excluded from reconstruction. This strategy does not interfere with scanning process and avoids prospective gating which is usually vulnerable to irregular breathing patterns. Since the scan duration is a continuous 8-min acquisition, the available data spanning the entire scan time are adequate to yield a quality phase reconstruction even with removal of some isolated data.

5. CONCLUSIONS

The recently developed self-gating-based *k*- space sorted 4D-MRI technique has been evaluated and compared with 4D-CT techniques using a MRI/CT compatible phantom. The 4D MRI technique provides a robust approach for accurately measuring phase-based target geometry while avoiding typical motion artifacts. Compared to 4D-CT, the current 4D-MRI technique demonstrates superior spatiotemporal resolution, and robust resistance to motion artifacts due to fast target motion and irregular breathing. The technique can be used extensively in abdominal targeting, motion gating, and toward implementing MRI-based adaptive radiotherapy.

[a] Author to whom correspondence should be addressed. Electronic mail: yong.yue@cshs.org

[1] S. Vedam, P. Keall, V. Kini, H. Mostafavi, H. Shukla, and R. Mohan, "Acquiring a four-dimensional computed tomography dataset using an external respiratory signal," Phys. Med. Biol. **48**, 45–62 (2003).

[2] D. Low, M. Nystrom, E. Kalinin, P. Parikh, J. Dempsey, J. Bradley, S. Mutic, S. Wahab, T. Islam, G. Christensen, D. Politte, and B. Whiting, "A method for the reconstruction of four-dimensional synchronized CT scans acquired during free breathing," Med. Phys. **30**, 1254–1263 (2003).

[3] P. Keall, "4-dimensional computed tomography imaging and treatment planning," Semin. Radiat. Oncol. **14**, 81–90 (2004).

[4] E. Rietzel, G. Chen, N. Choi, and C. Willet, "Four-dimensional image-based treatment planning: Target volume segmentation and dose calculation in the presence of respiratory motion," Int. J. Radiat. Oncol., Biol., Phys. **61**, 1535–1550 (2005).

[5] H. Hof, B. Rhein, P. Haering, A. Kopp-Schneider, J. Debus, and K. Herfarth, "4D-CT-based target volume definition in stereotactic radiotherapy of lung tumours: Comparison with a conventional technique using individual margins," Radiother. Oncol. **93**, 419–423 (2009).

[6] P. Keall, S. Vedam, R. George, and J. Williamson, "Respiratory regularity gated 4D CT acquisition: Concepts and proof of principle," Australas. Phys. Eng. Sci. Med. **30**, 211–220 (2007).

[7] T. Yamamoto, U. Langner, B. Loo, J. Shen, and P. Keall, "Retrospective analysis of artifacts in four-dimensional CT images of 50 abdominal and thoracic radiotherapy patients," Int. J. Radiat. Oncol., Biol., Phys. **72**, 1250–1258 (2008).

[8] M. Von Siebenthal, P. Cattin, U. Gamper, A. Lomax, and G. Székely, "4D MR imaging using internal respiratory gating," Med. Image Comput. Comput. Assist. Interv. **8**(Pt. 2), 336–343 (2005).

[9] J. Blackall, S. Ahmad, M. Miquel, J. McClelland, D. Landau, and D. Hawkes, "MRI-based measurements of respiratory motion variability and assessment of imaging strategies for radiotherapy planning," Phys. Med. Biol. **51**, 4147–4169 (2006).

[10] J. Dinkel, C. Hintze, R. Tetzlaff, P. Huber, K. Herfarth, J. Debus, H. Kauczor, and C. Thieke, "4D-MRI analysis of lung tumor motion in patients with hemidiaphragmatic paralysis," Radiother. Oncol. **91**, 449–454 (2009).

[11] C. Plathow, M. Klopp, M. Schoebinger, C. Thieke, C. Fink, M. Puderbach, S. Ley, M. Weber, A. Sandner, C. Claussen, F. Herth, S. Tuengerthal, H. Meinzer, and H. Kauczor, "Monitoring of lung motion in patients with malignant pleural mesothelioma using two-dimensional and three-dimensional dynamic magnetic resonance imaging: Comparison with spirometry," Invest. Radiol. **41**, 443–448 (2006).

[12] J. Tokuda, S. Morikawa, H. Haque, T. Tsukamoto, K. Matsumiya, H. Liao, K. Masamune, and T. Dohi, "Adaptive 4D MR imaging using navigator-based respiratory signal for MRI-guided therapy," Magn. Reson. Med. **59**, 1051–1061 (2008).

[13] J. Cai, Z. Chang, Z. Wang, P. Segars, and F. Yin, "Four-dimensional magnetic resonance imaging (4D-MRI) using image-based respiratory surrogate: A feasibility study," Med. Phys. **38**, 6384–6394 (2011).

[14] Y. Hu, S. Caruthers, D. Low, P. Parikh, and S. Mutic, "Respiratory amplitude guided 4-dimensional magnetic resonance imaging," Int. J. Radiat. Oncol., Biol., Phys. **86**, 198–204 (2013).

[15] E. Tryggestad, A. Flammang, S. Han-Oh, R. Hales, J. Herman, T. McNutt, T. Roland, S. Shea, and J. Wong, "Respiration-based sorting of dynamic MRI to derive representative 4D-MRI for radiotherapy planning," Med. Phys. **40**, 051909 (12pp.) (2013).

[16] M. Von Siebenthal, G. Székely, U. Gamper, P. Boesiger, A. Lomax, and P. Cattin, "4D MR imaging of respiratory organ motion and its variability," Phys. Med. Biol. **52**, 1547–1564 (2007).

[17] Y. Masuda and H. Haneishi, "4D MR imaging of respiratory organ motion using an intersection profile method," Proc. SPIE **7625**, 76250Z (2010).

[18] D. Han, J. Bayouth, S. Bhatia, M. Sonka, and X. Wu, "Characterization and identification of spatial artifacts during 4D-CT imaging," Med. Phys. **38**, 2074–2087 (2011).

[19] C. Hurkmans, M. Lieshout, D. Schuring, M. van Heumen, J. Cuijpers, F. Lagerwaard, J. Widder, U. van der Heide, and S. Senan, "Quality assurance of 4D-CT scan techniques in multicenter phase III trial of surgery versus stereotactic radiotherapy (radiosurgery or surgery for operable early stage (stage 1A) non-small-cell lung cancer [ROSEL] study)," Int. J. Radiat. Oncol., Biol., Phys. **80**, 918–927 (2011).

[20] Z. Deng, J. Pang, W. Yang, Y. Yue, R. Tuli, B. Fraass, D. Li, and Z. Fan, "Respiratory phase-resolved 3D MRI with isotropic high spatial resolution: Determination of the average breathing motion pattern for abdominal radiotherapy planning," Med. Phys. **41**, 473–474 (2014).

[21] Z. Fan, J. Pang, W. Yang, Y. Yue, R. Tuli, G. Xie, X. Bi, B. Fraass, and D. Li, "Respiratory phase-resolved 3D MRI with isotropic high spatial resolution: Determination of the average breathing motion pattern for abdominal radiotherapy planning," in *International Society for Magnetic Resonance in Medicine*, Milano, Italy (2014).

[22] Z. Deng, J. Pang, W. Yang, Y. Yue, B. Sharif, R. Tuli, D. Li, B. Fraass, and Z. Fan, "4D MRI using 3D radial sampling with respiratory self-gating to characterize temporal phase-resolved respiratory motion in the abdomen," Magn. Reson. Med. (2015) [Epub ahead of print].

[23] J. Pang, B. Sharif, R. Arsanjani, X. Bi, Z. Fan, Q. Yang, K. Li, D. Berman, and D. Li, "Accelerated whole-heart coronary MRA using motion-corrected sensitivity encoding with three-dimensional projection reconstruction," Magn. Reson. Med. **73**, 284–291 (2015).

[24] R. Chan, E. Ramsay, C. Cunningham, and D. Plewes, "Temporal stability of adaptive 3D radial MRI using multidimensional golden means," Magn. Reson. Med. **61**, 354–363 (2009).

[25] J. Pang, B. Sharif, Z. Fan, X. Bi, R. Arsanjani, D. Berman, and D. Li, "ECG and navigator-free four-dimensional whole-heart coronary MRA for simultaneous visualization of cardiac anatomy and function," Magn. Reson. Med. **72**, 1208–1217 (2014).

[26] P. Yushkevich, J. Piven, H. Hazlett, R. Smith, S. Ho, J. Gee, and G. Gerig, "User-guided 3D active contour segmentation of anatomical structures: Significantly improved efficiency and reliability," NeuroImage **31**, 1116–1128 (2006).

[27] J. Dempsey, D. Benoit, J. Fitzsimmons, A. Haghighat, J. Li, D. Low, S. Mutic, J. Palta, H. Romeijn, and G. Sjoden, "A device for realtime 3D image-guided IMRT," Int. J. Radiat. Oncol., Biol., Phys. **63**, S202 (2005).

[28] J. Lagendijk, B. Raaymakers, and M. Vulpen, "The magnetic resonance imaging-linac system," Semin. Radiat. Oncol. **24**, 207–209 (2014).

[29] P. Keall, M. Barton, and S. Crozier, "The Australian magnetic resonance imaging-linac program," Semin. Radiat. Oncol. **24**, 203–206 (2014).

[30] B. Fallone, "The rotating biplanar linac-magnetic resonance imaging system," Semin. Radiat. Oncol. **24**, 200–202 (2014).

[31] Y. Okamoto, K. Imanaka, T. Sakaguchi, T. Kushima, and M. Kono, "Fundamental study on development of MRI simulation system for radiotherapy planning," Int. J. Radiat. Oncol., Biol., Phys. **27**(Suppl. 1), 303 (1993).

[32] C. Rank, N. Hünemohr, A. Nagel, M. Röthke, O. Jäkel, and S. Greilich, "MRI-based simulation of treatment plans for ion radiotherapy in the brain region," Radiother. Oncol. **109**, 414–418 (2013).

[33] S. Devic, "MRI simulation for radiotherapy treatment planning," Med. Phys. **39**, 6701–6711 (2012).